American Mineralogist, Volume 93, pages 632–643, 2008

Thermal behavior of a Ti-rich phlogopite from Mt. Vulture (Potenza, Italy): An in situ X-ray single-crystal diffraction study

Gennaro Ventruti,[1] Michele Zema,[2,3] Fernando Scordari,[1,*] and Giuseppe Pedrazzi[4]

[1]Dipartimento Geomineralogico, Università degli Studi di Bari, Via E. Orabona 4, I-70125 Bari, Italy
[2]Dipartimento di Scienze della Terra, Università degli Studi di Pavia, via Ferrata 1, I-27100 Pavia, Italy
[3]CNR-IGG, Sezione di Pavia, via Ferrata 1, I-27100 Pavia, Italy
[4]Dipartimento di Sanità Pubblica, Sezione di Fisica, Plesso Biotecnologico Integrato, via Volturno 39, I-43100 Parma, Italy

Abstract

The structural evolution of a trioctahedral mica from Cava St. Antonio, Mt. Vulture, Potenza, Italy, has been studied in the temperature range 100–1023 K using in situ single-crystal X-ray diffraction techniques. The sample used shows a Ti-rich composition close to the phlogopite-annite join with the following crystal-chemical formula: $(K_{0.85}Na_{0.11}Ba_{0.03})(Al_{0.17}Mg_{1.98}Mn_{0.01}Fe^{2+}_{0.29}Fe^{3+}_{0.37}Ti_{0.18})(Si_{2.75}Al_{1.25})O_{10.66}(F_{0.13}OH_{1.20}Cl_{0.01})$. In the present study, the chemical and structural changes and the deprotonation process involved during heating have been characterized. Analysis of the data showed that *a*, *b*, and *c* cell parameters expand almost linearly up to 823 K, while the β angle remains constant. A sharp decrease in the unit-cell dimensions was observed at 873 and 1023 K. Linear trends obtained during reversal experiments from 1023 K to room temperature demonstrated the irreversibility of these events.

Structure refinements of single-crystal XRD data collected at 100, 200, 298, 473, 673, 873, and 1023 K converged to $2.14 \le R\ (\%) \le 8.47$, $2.47 \le R_w\ (\%) \le 10.83$. In the temperature range 100–673 K, the thermal expansion along the **c** direction is mainly due to interlayer thickness dilation. The tetrahedral ring approaches the ideal hexagonal shape with increasing temperature to match the expanding octahedral sheet. In the range 873–1023 K, a strong shrinking of the interlayer is associated with the shortening of the M1-O4 and M2-O4 distances and to the consequent reduction of octahedral thickness. Such structural features indicate the occurrence of Fe oxidation process, involving loss of structural H, which is responsible for a phase transition. Mössbauer spectroscopy supported this hypothesis.

Keywords: Trioctahedral mica, single-crystal X-ray diffraction, deprotonation, thermal expansion

Introduction

Micas are very common minerals occurring in a wide variety of geological environments. They are important because they control the introduction of H_2O into the mantle. This strongly influences melting conditions and other properties of the subcrustal material. High-temperature studies are mostly devoted to (1) understanding the mechanisms of storage and release of H_2O in micas under extreme conditions, through thermal activation, and (2) investigating the effects of the oxygen fugacity upon phase relation diagrams. Understanding the thermal behavior of this mineral family is crucial to provide a reliable basis for further interpretation and prediction of phase equilibria, phase transformations and most reactions occurring in a variety of rocks, and the development of geothermometers as well.

Several spectroscopic and structural studies have been performed on trioctahedral micas at high temperature, most of them on powdered samples. As concerns Fe-bearing phlogopites, complications arise from the multiple oxidation states of iron and the ability of the Fe-rich structure to compensate for oxidation or reduction. In this case, the modification of Fe-oxidation is shown by a marked change in slope of the lattice parameters and hence of the cell volume upon increasing *T*. However, the temperature range can be variable, depending on the rate of the change in *T* and the possible non-equilibrium conditions of the sample, and the particular environmental conditions of the process.

Takeda and Morosin (1975) first pioneered a high-temperature structural study of a synthetic fluorophlogopite single crystal. In their study the authors successfully related a geometrical model to deduce structural changes of the micas from the observed lattice expansion. They also observed a kink in the lattice parameter expansivities at 400 °C and a change in the expansion mode of Mg-octahedra. Takeda and Ross (1975) examined two polytypes ($1M$, $2M_1$) of Fe-rich phlogopites hydrogenated by a flow of hydrogen gas at 700 °C, while Ohta et al. (1982) used hot argon gas to produce a hydrogen-depleted and oxidized (oxy-mica) counterpart of each polytype for comparison. These studies clearly showed that interlayer separation is significantly affected by H content due to electrostatic repulsions between the interlayer cation and the H, in addition to cell parameter change caused by the reduction/oxidation process effects on the iron cation.

Rancourt et al. (2001) performed a detailed study, by means of a combination of several techniques, of the transformations annite → oxyannite, through the reaction $Fe^{2+} + OH^- \rightarrow Fe^{3+} +$

* E-mail: f.scordari@geomin.uniba.it

$O^{2-} + H\uparrow$, and oxyannite → ferryoxyannite through the reaction $3Fe^{2+} \rightarrow 2Fe^{3+} + {}^{VI}\square + Fe\uparrow$. Their analysis was corroborated by quantitative determination of the H content, precise ferrous/ferric ratio evaluation, and careful consideration of Fe oxide impurity phase, and structural test for the presence of octahedral vacancies.

About twenty years after Takeda and Morosin's structural investigation, Russell and Guggenheim (1999) examined by single-crystal X-ray diffraction the thermal behavior of a near end-member phlogopite up to 600 °C and a heat-treated Fe-rich phlogopite. In contrast to fluorophlogopite (Takeda and Morosin 1975), the OH-rich M-octahedra expand without changing shape, while heated Fe-rich phlogopite showed more flattened interlayer and octahedral sites over the unheated sample. Comodi et al. (1999) discussed the structural aspects observed in Fe-oxidation mechanisms in a synthetic Cs-tetra-ferriannite single crystal through bond-length changes and a kinetic study of cell parameters. Tutti et al. (2000) reported a powder diffraction study of a phlogopite from Pargas (Finland) at high temperature. They observed that the linear trends of lattice parameters *a*, *b*, and *c,* as a function of temperature, broke at 400 °C into two regions exhibiting quite different thermal expansion coefficients. From TGA and DTG measurements such a behavior upon heating is presumably related to the oxidation of Fe^{2+}, which takes place at about 500–600 °C, and is accomplished by dehydrogenation of hydroxyls coordinated to Fe. Chon et al. (2003) performed an in situ and ex situ high-temperature investigation of a Fe-bearing phlogopite using neutron powder diffraction. They observed mechanisms of Fe oxidation associated with deprotonation only for the ex situ heat-treated Fe-rich phlogopite. A recent study (Chon et al. 2006) combined in situ high-temperature neutron powder diffraction with ex situ high-temperature FTIR spectroscopy and showed that Fe-oxydation-deprotonation processes occurred at around 500 °C.

In this work, the results of low-temperature (LT) and room-temperature (RT) high-resolution XRD structural analyses and high-temperature (HT) in situ investigations on a natural phlogopite of composition close to phlogopite-annite join are reported. Titanium-rich phlogopites from the same locality were previously investigated through a multianalytical approach (Scordari et al. 2006). The present study has mainly two goals: (1) to investigate in detail how the structure of trioctahedral micas of complex composition responds to heating and (2) to examine the inter-relationship between Fe-oxydation and structural H loss. In addition, with reference to the last item, this study aims to check the compositional disorder of Fe^{2+} over octahedral sites observed by Scordari et al. (2006).

Experimental methods

Sample and chemical composition

A single crystal of 1*M*-polytype mica from Cava S. Antonio (Mt. Vulture, Italy), labeled SA, having dimension 0.50 × 0.36 × 0.02 mm and showing negligible effects of diffuse streaks parallel to **c*** was selected for the present study.

Similar SA samples have been recently subject to a multi-technical investigation by Scordari et al. (2006). According to the authors these trioctahedral micas belong to the phlogopite-annite solid solution [annitic component $Fe_{tot}/(Fe_{tot} + Mg) \approx 0.25$] with Ti ≈ 0.20 atoms per formula unit (apfu) and have a quite homogeneous composition. Combined results from this multi-technical approach allowed these authors to assess unambiguously that both ${}^{VI}Ti^{4+}$ and ${}^{VI}Fe^{3+}$ enter the structure through R-oxy substitution mechanisms involving deprotonation at O4.

The atomic ratios for data from single crystals have been calculated on the basis of 12(O, OH, Cl, F), assuming all Ti as Ti^{4+}, using the Fe^{2+}/Fe^{3+} ratios provided from Mössbauer investigation (Scordari et al. 2006) and total H content as obtained by C-H-N elemental analysis.

Electron microprobe analyses (EMPA) on the same crystals used for single-crystal X-ray diffraction experiments were obtained with a Cameca SX-50 electron microprobe at the Istituto di Geologia Ambientale e Geoingegneria (IGAG), CNR. The analyses were carried out in the full wavelength dispersive (WDS) mode. Operating conditions were 15 kV accelerating voltage, 15 nA beam current, 15 s peak counting times, and 10 µm beam size. The following standards were employed: jadeite (Na), periclase (Mg), wollastonite (Si and Ca), rutile (Ti), corundum (Al), magnetite (Fe), orthoclase (K), barite (Ba), fluoro-phlogopite (F), and sylvite (Cl). A conversion from X-ray counts to oxide weight percentages (wt%) was obtained with the PAP data reduction method (Pouchou and Pichoir 1985).

The averaged results of EMPA analyses and the crystal-chemical formula in apfu, obtained by combining EMPA data with the results of Mössbauer spectroscopy and C-H-N elemental analysis, are listed in Table 1. EMPA data represent the average over 8 spots. The crystal-chemical formula calculated on the basis of these results is $(K_{0.85}Na_{0.11}Ba_{0.03})(Al_{0.17}Mg_{1.98}Mn_{0.01}Fe^{2+}_{0.29}Fe^{3+}_{0.37}Ti_{0.18})(Si_{2.75}Al_{1.25})O_{10.66}(F_{0.13}OH_{1.20}Cl_{0.01})$.

Mössbauer spectroscopy

The Mössbauer spectrum of the untreated sample has been reported by Scordari et al. (2006). This investigation has ascertained that trioctahedral micas from intermediate Mt. Vulture volcanics (SA sample) are characterized by Fe^{2+} = 44%, Fe^{3+} = 56%. Typical features of Mössbauer spectrum of SA micas are displayed in Figure 1a, namely three absorption bands at approximately –0.2, 1.0, and 2.3 mm/s that correspond, respectively, to (1) the sum of low energy lines of ${}^{VI}Fe^{2+}$ and ${}^{VI}Fe^{3+}$ doublets; (2) the high energy line of the ${}^{VI}Fe^{3+}$ doublet; and (3) the high energy component of the ${}^{VI}Fe^{2+}$ doublet. No shoulder at ~0.5 mm/s (evidence for the occurrence of tetrahedral Fe^{3+}) was observed.

In this work, the Mössbauer spectrum was recorded on ~50 mg of powdered SA sample that was preliminarily heated in air at 900 K for about 6 h and quenched by simply pulling it out of the furnace. Transition ${}^{57}Fe$ Mössbauer spectra were recorded at room and liquid nitrogen (77 K) temperature using a conventional Mössbauer apparatus in transmission geometry with a ${}^{57}Co$ (in a rhodium matrix) single line thin source (~1 GBq). The spectrometer operated in constant acceleration mode with a symmetric triangular velocity shape and a multi-channel analyzer with 512 channels. The velocity range was ±7 mm/s and the velocity was calibrated against ${}^{57}Fe$ enriched α-Fe. The two Mössbauer spectra of the heat-treated sample do not differ significantly (Fig. 1b displays the one recorded at room temperature). They

Table 1. Chemical composition of sample SA (apfu determined by combining EMPA, Mössbauer, and C-H-N elemental analysis)

Oxide (wt%)		Apfu	
SiO_2	36.76(19)	Si	2.751(7)
TiO_2	3.21(7)	Al	1.249(7)
Al_2O_3	16.13(14)	ΣT	4.000
Cr_2O_3	0.02(2)		
FeO_{tot}	10.42(17)	Al	0.173(8)
MnO	0.17(7)	Mg	1.981(12)
MgO	17.76(14)	Fe^{2+}	0.287(5)
BaO	0.95(5)	Fe^{3+}	0.365(6)
CaO	0.05(1)	Ti	0.181(3)
Na_2O	0.74(9)	Mn	0.011(4)
K_2O	8.92(9)	ΣOct.	2.998
F	0.55(14)		
Cl	0.04(1)	K	0.850(7)
Total	95.72(45)	Na	0.107(13)
		Ba	0.028(1)
FeO*	4.59	Ca	0.003(1)
Fe_2O_3*	6.49	ΣInt.	0.988
H_2O†	2.41(6)		
Total	98.79	OH	1.203(5)
		F	0.130(31)
		Cl	0.005(1)
		ΣA	1.338

Notes: T = Tetrahedral; Oct. = Octahedral; Int. = Interlayer; A = Anion.
* Recalculated from Mössbauer analysis.
† From C-H-N elemental analysis.

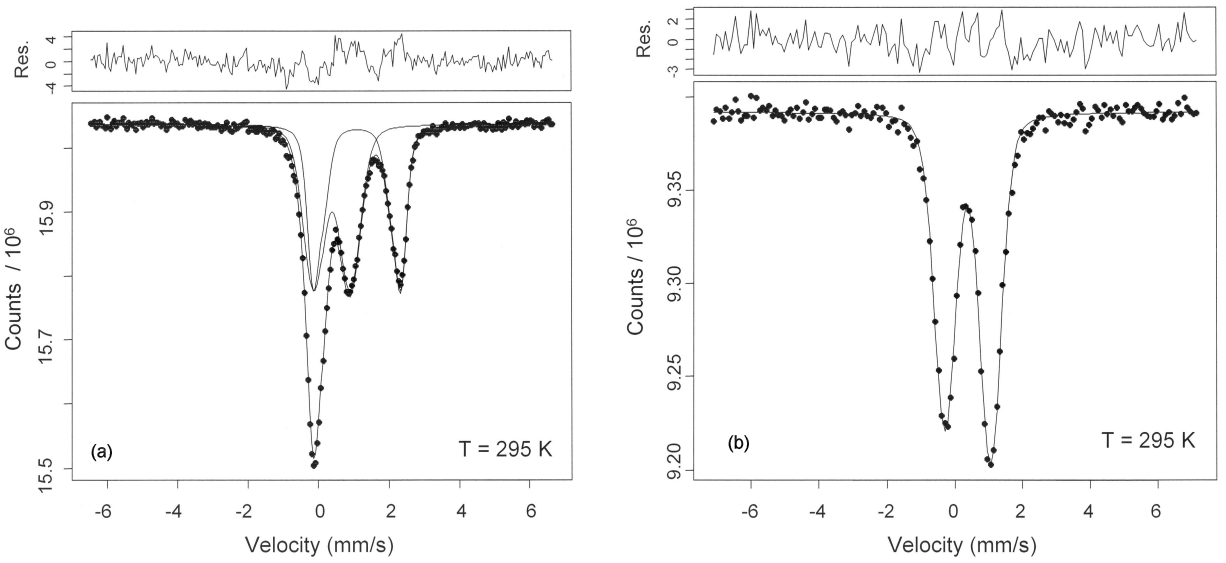

FIGURE 1. Room-temperature QSD fitted Mössbauer spectra for SA mica. (**a**) Untreated sample; (**b**) heat-treated sample at T = 900 K.

show two slightly asymmetric absorption bands at around –0.2 and 1.0 mm/s. This asymmetry is attributable to texture effects in the specimen (Rancourt et al. 1994b). Spectra were fitted according to Voigt-function-based quadrupole splitting distribution (QSD) method (Rancourt and Ping 1991; Rancourt et al. 1994a, 1994b) using software "Recoil" (Lagarec and Rancourt 1998). More details about experimental conditions and data analysis are described in Schingaro et al. (2005). From the results of the fitting procedure it can be argued that all ferrous iron is transformed to the trivalent state. The crystal-chemical formula of the heat-treated sample calculated on the basis of these results is $(K_{0.85}Na_{0.11}Ba_{0.03})(Mg_{1.98}Al_{0.17}Mn_{0.01}Fe^{3+}_{0.66}Ti_{0.18})(Si_{2.75}Al_{1.25})O_{10.95}(OH_{0.91}F_{0.13}Cl_{0.01})$.

The results of n_1-n_2 fittings, where n_1 and n_2 are the numbers of assumed QSD Gaussian components for $^{VI}Fe^{2+}$ and $^{VI}Fe^{3+}$ sites, respectively, are reported in Table 2. A^-/A^+ ratios were allowed to vary during fitting to take into account non-ideal orientation randomness of the sample. The fitting parameters are consistent with those reported in the literature for synthetic and natural trioctahedral micas (Redhammer 1998; Rancourt et al. 1993, 1994a; Dyar 2002).

Single-crystal X-ray diffraction

Two different strategies of data collection and lattice parameters measurement by single-crystal X-ray diffraction (SC-XRD) were used. A Bruker AXS X8 APEX automated diffractometer equipped with a four-circle Kappa goniometer and a CCD detector was used for low- and room-temperature experiments, while a conventional Philips PW1100 four-circle diffractometer with point counter detector was used for the high-temperature studies.

SC-XRD: CCD detector. In situ LT and RT data collections of the untreated sample, as well as a RT data collection of the same crystal after the heating cycle, were performed at 50 kV and 30 mA by means of graphite-monochromatized Mo$K\alpha$ radiation (λ = 0.71073 Å). The crystal was cooled to 100(1) and 200(1) K using a Bruker Kryoflex device. The temperature was stable within 0.1 K (monitored every 30 s) for the duration of the experiments. At least 1 h was allowed for thermal equilibration at each temperature.

For each measurement, three sets of 12 frames acquired with 0.5° φ rotation were used for the initial unit-cell determinations. The collection strategy was then optimized by the Apex program suite (Bruker 2001); the intensities of reflections of the whole Ewald sphere ($\pm h, \pm k, \pm l$) were accurately recorded by a combination of several ω and φ rotation sets with 0.5° scan width. For each data collection, a total of 1971 frames (512 × 512 pixels resolution) were recorded with a crystal-to-detector distance of 40 mm and a 10 s/frame exposure time. The package SAINT-IRIX (Bruker 2003) was used for data reduction, including intensity integration; moreover the data were corrected for Lorentz, polarization, background effects, and scale variation. The final unit-cell parameters were obtained from the *xyz* centroids of the measured reflections after integration and are reported in Table 3, while details on data collections are in Table 4. A semi-empirical absorption correction based on the determination of transmission factors for equivalent reflections (Blessing 1995) was applied by means of the SADABS software (Sheldrick 2003).

SC-XRD: point detector. In situ high-temperature lattice parameters measurements and intensity data collections were carried out at 55 kV and 30 mA by means of graphite-monochromatized Mo$K\alpha$ radiation (λ = 0.71073 Å) using a homemade U-shaped microfurnace with a K-type thermocouple. The selected crystal was inserted into a sealed quartz capillary (0.5 mm Ø) and kept in position by means of quartz wool. A graphite fragment was inserted into the quartz capillary at ~1.5 cm from the crystal to prevent early oxidation of the sample.

Unit-cell parameters were measured at regular intervals from room temperature up to 1023 K by means of a least-squares procedure based on the Philips LAT routine over 35 to 52 d*-spacings, each measured considering all the reflections in the range $3° < \theta < 25°$. Unit-cell parameters obtained at the different temperatures are reported in Table 3. At each temperature, measurements were taken after about 30 min to allow for thermal equilibration of the sample. The decrease of cell dimensions observed at 873 K was followed by continuously measuring lattice parameters by centering 25 reflections. When equilibrium was reached a new accurate determination of unit-cell lengths was carried out by the LAT procedure.

Reversal experiments were then performed by measuring unit-cell parameters from 1023 K down to room temperature at regular intervals. The obtained values are reported in Table 3 as well. At the end of the high-temperature study, the crystal was removed from the quartz capillary and mounted again on a glass fiber for a new structural investigation under ambient conditions by the CCD diffractometer (see above).

XRD intensity data were collected at 473, 673, 873, and 1023 K. In particular, at 873 K two data collections were performed at different times. Horizontal and vertical apertures were 2.0 and 1.5°, respectively. The equivalent reflections hkl and $h\bar{k}l$ were measured in the ω-2θ scan mode in the 2–26.5 °θ range, because the microfurnace itself limits the angular region to these values. Three standard reflections were collected every 200 reflections during data collection to monitor crystal and electronic stability. X-ray diffraction intensities were obtained by measuring step-scan profiles and analyzing them by the Lehman and Larsen (1974) σ_I/I method, as modified by Blessing et al. (1974). Intensities were corrected for absorption using the semi-empirical ψ-scan method of North et al. (1968).

Structure refinements. All the structure refinements were carried out in space group $C2/m$ using the program CRYSTALS (Betteridge et al. 2003) starting from the data of Hazen and Burnham (1973). Scattering curves for fully ionized chemical species were used for non-tetrahedral sites, whereas ionized vs. neutral scattering curves were used for Si and O (Hawthorne et al. 1995). Only reflections with $I > 3\sigma_I$ were considered suitable for the structure refinements. Refined parameters were scale factor, atomic positions, cations occupancies, and atomic displacement factors (anisotropic at LT and RT; isotropic at HT). Difference-Fourier maps calculated at the end of the low- and room-temperature refinements revealed the presence of a peak located at the expected position for the hydrogen atoms, at ~0.72–0.77 Å from the O4 oxygen. When H position was included in the last cycles of these

TABLE 2. Mössbauer parameters obtained by QSD method

	T (K)	χ^2	Species	δ_0† (mm/s)	A^-/A^+	ΔE_Q (mm/s)	σ	P (%)	A (%)
SA	295	2.19	Fe^{2+}	1.112	1‡	1.950	0.289	35	43.9(4)
				1.112	1‡	2.516	0.228	65	
			Fe^{3+}	0.393	1‡	1.023	0.523	100‡	56.1(4)
SA*	295	1.42	Fe^{3+}	0.387	0.904	1.358	0.556	100‡	100.00(–)
SA*	77	1.190	Fe^{3+}	0.481	0.913	1.360	0.552	100‡	100.00(–)

* Powder sample after heating cycle.
† $\delta_1 = 0$ during fitting.
‡ Fixed parameter.

TABLE 3. Unit-cell parameters of 1*M* phlogopite SA from 100 to 1023 K

T (K)	*a* (Å)	*b* (Å)	*c* (Å)	β (°)	*V* (Å³)
CCD measurements					
100	5.3278(2)	9.2225(3)	10.2087(3)	100.031(2)	493.94(3)
200	5.3310(1)	9.2298(3)	10.2217(3)	100.031(2)	495.26(2)
298	5.3365(1)	9.2438(2)	10.2331(3)	100.031(2)	497.08(2)
298*	5.3134(3)	9.1997(5)	10.1558(6)	99.988(3)	488.91(5)
"Heating-up" experiments					
298	5.3275(11)	9.2265(25)	10.2200(40)	100.013(3)	494.70(6)
373	5.3320(6)	9.2360(15)	10.2320(22)	100.031(1)	496.19(2)
473	5.3400(12)	9.2470(26)	10.2465(41)	100.055(3)	498.19(6)
523	5.3425(7)	9.2545(14)	10.2515(16)	100.043(1)	499.09(1)
573	5.3467(6)	9.2646(12)	10.2592(13)	100.082(1)	500.34(1)
623	5.3508(7)	9.2697(13)	10.2661(17)	100.073(1)	501.35(1)
673	5.3526(6)	9.2727(10)	10.2787(15)	100.069(1)	502.31(1)
723	5.3559(5)	9.2818(9)	10.2823(13)	100.044(1)	503.32(1)
773	5.3578(6)	9.2866(11)	10.2929(14)	100.075(1)	504.23(1)
823	5.3596(6)	9.2924(11)	10.2979(15)	100.050(2)	505.00(2)
873	5.3583(11)	9.2866(14)	10.2960(25)	100.081(3)	504.44(4)
873†	5.3560(10)	9.2798(14)	10.2863(25)	100.051(2)	503.41(3)
923	5.3594(10)	9.2857(14)	10.2908(22)	100.036(1)	504.29(2)
973	5.3603(8)	9.2867(12)	10.2986(23)	100.026(1)	504.83(2)
1023	5.3621(12)	9.2897(18)	10.2986(29)	100.064(3)	505.10(6)
1023‡	5.3577(11)	9.2807(20)	10.2832(36)	99.996(2)	503.55(4)
Reversal experiments					
1023§	5.3595(7)	9.2830(9)	10.2842(20)	100.016(12)	503.86(1)
973	5.3549(8)	9.2766(10)	10.2761(20)	99.988(12)	502.73(1)
873	5.3495(9)	9.2680(14)	10.2573(22)	100.024(14)	500.79(2)
773	5.3441(9)	9.2578(16)	10.2401(23)	100.049(14)	498.85(2)
673	5.3395(11)	9.2486(16)	10.2170(26)	100.001(26)	496.88(4)
573	5.3330(7)	9.2372(13)	10.2044(21)	100.028(12)	495.01(2)
473	5.3252(9)	9.2272(16)	10.1847(20)	100.018(12)	492.81(2)
373	5.3199(8)	9.2119(14)	10.1691(20)	100.029(13)	490.74(2)
298	5.3160(7)	9.2043(12)	10.1613(17)	100.060(10)	489.38(1)

Note: Standard deviations are in parentheses.
* At the end of the high-temperature study.
† 14 h after previous measurements at the same temperature.
‡ 48 h after previous measurements at the same temperature.
§ 12 h after previous measurements at the same temperature.

TABLE 4. Details on data collections and structure refinements of 1*M* phlogopite sample SA at different temperatures

	100 K	200 K	298 K	473 K	673 K	873 K	873 K†	1023 K	298 K*
Diffractometer type	X8 APEX	X8 APEX	X8 APEX	PW1100	PW1100	PW1100	PW1100	PW1100	X8 APEX
θ range	2–44.48°	2–44.14°	2–47.38°	2–26.50°	2–26.50°	2–26.50°	2–26.50°	2–26.50°	2–46.99°
Indexes ranges	$-10 \le h \le 9$	$-10 \le h \le 9$	$-11 \le h \le 10$	$-6 \le h \le 6$	$-6 \le h \le 6$	$-6 \le h \le 6$	$-6 \le h \le 6$	$-6 \le h \le 6$	$-10 \le h \le 10$
	$-17 \le k \le 11$	$-17 \le k \le 11$	$-18 \le k \le 12$	$-11 \le k \le 11$	$-11 \le k \le 11$	$-11 \le k \le 11$	$-11 \le k \le 11$	$-11 \le k \le 11$	$-18 \le k \le 18$
	$-20 \le l \le 20$	$-20 \le l \le 20$	$-21 \le l \le 21$	$0 \le l \le 12$	$0 \le l \le 12$	$0 \le l \le 12$	$0 \le l \le 12$	$0 \le l \le 12$	$-19 \le l \le 20$
Refl. meas./unique	17014/2017	17060/2060	18958/2329	2212/555	2212/555	2229/561	2200/553	2200/553	6816/2270
R_{int}‡	0.0321	0.0302	0.0258	0.1109	0.1109	0.1180	0.1147	0.1199	0.0246
Refl. used ($I > 3\sigma_I$)	1344	1303	1415	320	300	260	264	252	1126
Refined parameters	68	68	68	38	38	38	38	38	68
GooF‡	0.83	0.85	0.89	1.02	1.03	0.97	0.96	0.96	1.02
R_1 (on *F*)‡	0.0214	0.0220	0.0235	0.0579	0.0716	0.0847	0.0816	0.0695	0.0528
wR_1 (on *F*)‡	0.0247	0.0250	0.0256	0.0774	0.0955	0.1083	0.1038	0.0897	0.0665
wR_2 (on F^2)‡	0.0488	0.0493	0.0508	0.1526	0.1895	0.2142	0.2040	0.1763	0.1298
$(\Delta/\sigma)_{max}$	0.007	0.007	0.006	0.005	0.006	0.004	0.004	0.005	0.007
$\Delta\rho_{min}$, $\Delta\rho_{max}$ (e/Å³)	–0.28, 0.70	–0.28, 0.63	–0.50, 0.87	–1.13, 1.68	–1.18, 2.11	–1.26, 2.11	–1.20, 2.21	–1.01, 1.59	–1.09, 2.01

* At the end of the high-temperature study.
† 14 h after previous measurement at the same temperature.
‡ $R_{int} = \Sigma|F_o^2 - \langle F_o^2 \rangle|/\Sigma F_o^2$; GooF = $\{\Sigma[w(F_o^2 - F_c^2)^2]/(n-p)\}^{0.5}$, where *n* is the number of reflections, and *p* is the total number of parameters refined. $R_1 = \Sigma||F_o| - |F_c||/\Sigma|F_o|$; $wR_1 = \Sigma w||F_o| - |F_c||/\Sigma w|F_o|$; $wR_2 = \{\Sigma[w(F_o^2 - F_c^2)^2]/\Sigma[w(F_o^2)^2]\}^{1/2}$.

refinements, all final difference-Fourier maps became featureless.

The relevant agreement indexes and details of each refinement are reported in Table 4. Final atomic coordinates, site occupancies, and anisotropic and isotropic displacement parameters are given in Tables 5a and 5b for low- and high-temperature data sets, respectively. Selected interatomic bond distances in Å are listed in Table 6, whereas the distortion parameters commonly used in crystal chemical studies on micas are reported in Table 7. Finally, mean atomic numbers and octahedral and tetrahedral distances as obtained from structure refinements are compared in Table 8 to those calculated from chemical analyses using Shannon's (1976) radii and a mean anion radius according to Kogarko et al. (2005).

RESULTS

Variations of unit-cell parameters with *T*

The variations of unit-cell parameters and the resulting cell volume of SA phlogopite as a function of temperature are plotted in Figure 2. The β angle remains constant within the uncertainty of our measurements in the whole temperature range investigated (see data in Table 3) and hence is not reported in the figure. The two data sets at low and high temperature, respectively, obtained by a diffractometer with CCD detector and a conventional diffractometer, were normalized on the basis of the lattice parameters measured at room temperature. These are slightly different because of different peak position determination by point counter or area detectors. In spite of these instrumental differences, the temperature dependence of unit-cell parameters of SA sample shows a distinct linear behavior up to 823 K with a slight deviation from linearity at low temperature. The thermal expansion coefficients over the range 298–823 K, determined by least-squares linear regression analysis, are $\alpha_a = 1.24(4) \times 10^{-5}$/K, $\alpha_b = 1.40(4) \times 10^{-5}$/K, $\alpha_c = 1.47(4) \times 10^{-5}$/K, $\alpha_V = 4.10(4) \times 10^{-5}$/K. Axial expansion is slightly anisotropic with $\alpha_a:\alpha_b:\alpha_c = 1:1.13:1.19$. Quantitative estimation of structure-controlled thermal expansion anisotropies was derived using the formalism of Schneider and Eberhard (1990): $A = (|\alpha_b - \alpha_c| + |\alpha_b - \alpha_a| + |\alpha_c - \alpha_a|) \times 10^{+6}$, which yielded a value of 4.60 K^{-1}.

As evident from Figure 2, an abrupt discontinuity occurs at $T = 873$ K when a significant contraction of cell volume is observed. By increasing the temperature up to 1023 K, lattice parameters seem to expand again at almost the same rate as in the 100–823 K range, and at 1023 K subsequent measurements carried out at different times show a new contraction of the unit cell. Since only a single measurement was performed both at 923 and 973 K, we cannot establish whether these measurements represent stable structural states at these temperatures.

The decrease in the unit-cell volume during cooling is irreversible. Unit-cell parameters measured from 1023 K down to room temperature under "cooling-down" conditions lie in fact on straight lines that are fairly parallel to those obtained in the temperature range RT–823 K under "heating-up" conditions. Thermal expansion coefficients obtained on these data are $\alpha_a = 1.11(2) \times 10^{-5}$/K, $\alpha_b = 1.16(3) \times 10^{-5}$/K, $\alpha_c = 1.71(4) \times 10^{-5}$/K, $\alpha_V = 4.03(2) \times 10^{-5}$/K, with $\alpha_a:\alpha_b:\alpha_c = 1:1.05:1.54$, and anisotropic coefficient $A = 12$ K^{-1}.

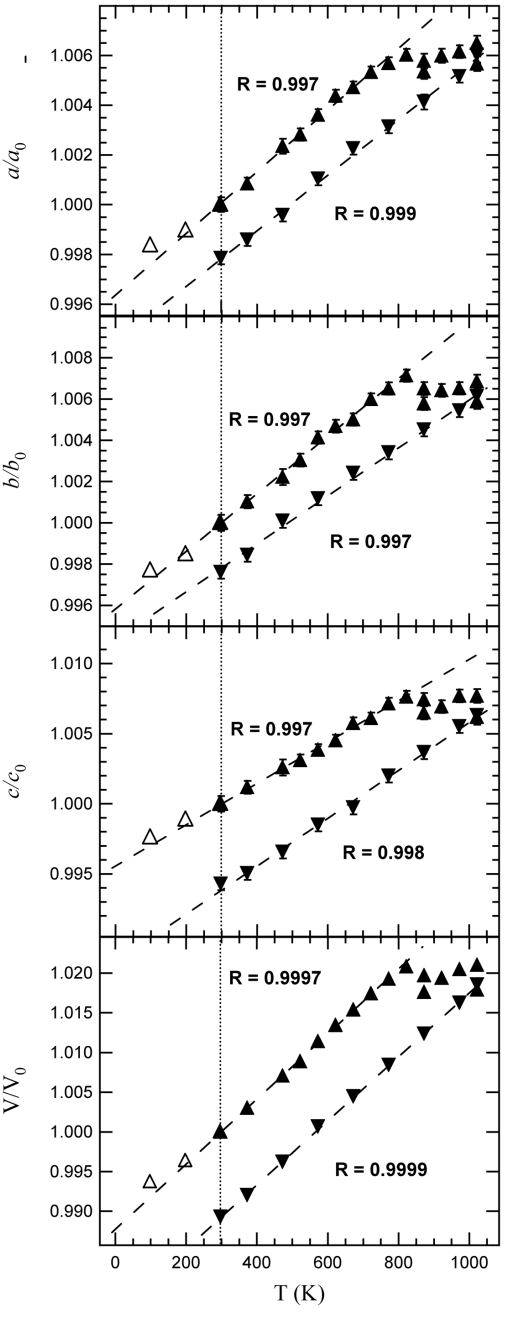

FIGURE 2. Variations of unit-cell parameters and cell volume with temperature. Triangles up = heating up experiments; triangles down = reversal experiments; open triangles = low-temperature data obtained by diffractometer with CCD detector. The dotted line denotes 298 K. Statistical tests R for linear regressions across 298–823 K temperature range are reported. The vertical size of the symbols exceeds the uncertainties in V/V_0.

Structural modifications

Bond lengths and geometrical parameters were derived from the structure refinements at 100, 200, 298, 473, 673, 873, and 1023 K (Tables 6 and 7). In most cases structural modifications with temperature reflect the same behavior exhibited by unit-cell parameters, with continuous and fairly linear trends from 100 up to 873 K where an abrupt discontinuity occurs.

Polyhedral volumes as a function of temperature are reported in Figure 3. The tetrahedral volume (Fig. 3a) exhibits a small linear contraction in the range 100–673 K as the result of the

TABLE 5A. Crystallographic coordinates, occupancies, equivalent isotropic (Å^2), and anisotropic displacement parameters

Atom	*x*	*y*	*z*	Occupancy	$U_{iso/equiv}$	U_{11}	U_{22}	U_{33}	U_{23}	U_{13}	U_{12}
100 K											
K	0.0000	0.5000	0.0000	1.0276(4)	0.0172	0.01597(17)	0.01614(18)	0.0197(2)	0.0000	0.00382(14)	0.0000
M1(Mg)	0.0000	0.0000	0.5000	0.7408(4)	0.0063	0.00543(16)	0.00495(17)	0.00922(19)	0.0000	0.00292(13)	0.0000
M1(Fe)	0.0000	0.0000	0.5000	0.2592(3)	0.0063	0.00543(16)	0.00495(17)	0.00922(19)	0.0000	0.00292(13)	0.0000
M2(Mg)	0.0000	0.33520(4)	0.5000	0.7393(4)	0.0072	0.00423(10)	0.00967(13)	0.00774(12)	0.0000	0.00103(9)	0.0000
M2(Fe)	0.0000	0.33520(4)	0.5000	0.2607(4)	0.0072	0.00423(10)	0.00967(13)	0.00774(12)	0.0000	0.00103(9)	0.0000
Si	0.07495(4)	0.16686(3)	0.22520(3)	0.9834(5)	0.0067	0.00575(8)	0.00654(9)	0.00789(9)	0.00018(8)	0.00150(7)	0.00005(7)
O1	0.33269(13)	0.22311(8)	0.16797(7)	1.0000(4)	0.0136	0.0127(3)	0.0173(3)	0.0112(3)	–0.0022(3)	0.0031(2)	–0.0035(2)
O2	0.0019(2)	0.0000	0.16889(10)	1.0000(4)	0.0136	0.0180(4)	0.0111(4)	0.0109(4)	0.0000	0.0000(3)	0.0000
O3	0.13082(12)	0.16751(7)	0.39136(7)	1.0000(4)	0.0084	0.0081(2)	0.0084(2)	0.0085(2)	0.0001(2)	0.00135(18)	0.00019(19)
O4	0.13190(17)	0.5000	0.39874(9)	1.0000(3)	0.0086	0.0083(3)	0.0107(4)	0.0069(4)	0.0000	0.0015(3)	0.0000
H	0.111(6)	0.5000	0.319(3)	0.5931(5)	0.0086						
200 K											
K	0.0000	0.5000	0.0000	1.0279(5)	0.0237	0.0232(2)	0.0235(2)	0.0245(2)	0.0000	0.00481(17)	0.0000
M1(Mg)	0.0000	0.0000	0.5000	0.7365(8)	0.0080	0.0067(2)	0.0063(2)	0.0112(2)	0.0000	0.0032(1)	0.0000
M1(Fe)	0.0000	0.0000	0.5000	0.2635(5)	0.0080	0.0067(2)	0.0063(2)	0.0112(2)	0.0000	0.0032(1)	0.0000
M2(Mg)	0.0000	0.33520(4)	0.5000	0.7322(4)	0.0088	0.0055(1)	0.0108(1)	0.0097(1)	0.0000	0.00113(9)	0.0000
M2(Fe)	0.0000	0.33520(4)	0.5000	0.2678(4)	0.0088	0.0055(1)	0.0108(1)	0.0097(1)	0.0000	0.00113(9)	0.0000
Si	0.07508(4)	0.16685(3)	0.22553(3)	0.9815(9)	0.0078	0.00691(9)	0.0074(1)	0.0092(1)	0.00014(9)	0.00165(7)	0.00007(8)
O1	0.33154(14)	0.22433(9)	0.16831(7)	1.0000(4)	0.0158	0.0148(3)	0.0204(4)	0.0129(3)	–0.0026(3)	0.0037(2)	–0.0046(3)
O2	0.0046(2)	0.0000	0.16928(11)	1.0000(4)	0.0160	0.0217(5)	0.0124(5)	0.0130(4)	0.0000	–0.0001(4)	0.0000
O3	0.13087(12)	0.16746(7)	0.39151(7)	1.0000(4)	0.0095	0.0093(2)	0.0097(3)	0.0097(2)	0.0002(2)	0.0015(2)	0.0003(2)
O4	0.13181(17)	0.5000	0.39884(10)	1.0000(4)	0.0099	0.0094(3)	0.0113(4)	0.0091(4)	0.0000	0.0017(3)	0.0000
H	0.107(10)	0.5000	0.327(5)	0.5946(10)	0.0099						
298 K											
K	0.0000	0.5000	0.0000	1.0253(6)	0.0309	0.0316(3)	0.0304(3)	0.0310(3)	0.0000	0.0059(2)	0.0000
M1(Mg)	0.0000	0.0000	0.5000	0.7381(8)	0.0096	0.0087(2)	0.0068(2)	0.0136(2)	0.0000	0.0036(2)	0.0000
M1(Fe)	0.0000	0.0000	0.5000	0.2619(5)	0.0096	0.0087(2)	0.0068(2)	0.0136(2)	0.0000	0.0036(2)	0.0000
M2(Mg)	0.0000	0.33517(3)	0.5000	0.7326(8)	0.0105	0.0074(1)	0.0116(1)	0.0123(1)	0.0000	0.0018(1)	0.0000
M2(Fe)	0.0000	0.33517(3)	0.5000	0.2674(6)	0.0105	0.0074(1)	0.0116(1)	0.0123(1)	0.0000	0.0018(1)	0.0000
Si	0.07523(4)	0.16684(2)	0.22587(3)	0.9811(9)	0.0093	0.00874(9)	0.00819(9)	0.0110(1)	0.00005(9)	0.00215(7)	0.00008(8)
O1	0.33016(14)	0.22599(9)	0.16870(7)	1.0000(7)	0.0188	0.0178(3)	0.0235(3)	0.0158(3)	–0.0031(3)	0.0047(3)	–0.0063(3)
O2	0.0080(2)	0.0000	0.16946(11)	1.0000(7)	0.0188	0.0265(5)	0.0128(4)	0.0159(5)	0.0000	0.0001(4)	0.0000
O3	0.13081(12)	0.16746(7)	0.39157(7)	1.0000(7)	0.0109	0.0114(2)	0.0109(2)	0.0108(2)	–0.0003(2)	0.0022(2)	–0.0002(2)
O4	0.13192(18)	0.5000	0.39889(10)	1.0000(7)	0.0121	0.0115(4)	0.0132(3)	0.0116(4)	0.0000	0.0019(3)	0.0000
H	0.113	0.5000	0.325(5)	0.5936(10)	0.0121						
298 K after reversal experiment											
K	0.0000	0.5000	0.0000	1.0217(8)	0.0287	0.0259(6)	0.0264(6)	0.0342(8)	0.0000	0.0064(5)	0.0000
M1(Mg)	0.0000	0.0000	0.5000	0.73956(19)	0.0127	0.0104(4)	0.0097(4)	0.0188(6)	0.0000	0.0048(4)	0.0000
M1(Fe)	0.0000	0.0000	0.5000	0.26044(19)	0.0127	0.0104(4)	0.0097(4)	0.0188(6)	0.0000	0.0048(4)	0.0000
M2(Mg)	0.0000	0.34126(9)	0.5000	0.73765(19)	0.0104	0.0050(2)	0.0117(3)	0.0132(3)	0.0000	0.0010(2)	0.0000
M2(Fe)	0.0000	0.34126(9)	0.5000	0.26235(19)	0.0104	0.0050(2)	0.0117(3)	0.0132(3)	0.0000	0.0010(2)	0.0000
Si	0.07398(11)	0.16718(7)	0.22456(7)	0.9792(9)	0.0093	0.0076(2)	0.0082(2)	0.0122(3)	0.0000(2)	0.00209(19)	0.00020(19)
O1	0.3280(4)	0.2262(2)	0.1669(2)	1.0000(7)	0.0182	0.0155(7)	0.0219(9)	0.0177(8)	–0.0040(8)	0.0046(6)	–0.0053(6)
O2	0.0083(6)	0.0000	0.1683(3)	1.0000(7)	0.0180	0.0232(12)	0.0123(10)	0.0173(12)	0.0000	0.0003(10)	0.0000
O3	0.1304(3)	0.16860(17)	0.39181(18)	1.0000(7)	0.0104	0.0083(5)	0.0091(5)	0.0138(6)	–0.0004(6)	0.0019(5)	0.0001(5)
O4	0.1351(5)	0.5000	0.4005(3)	1.0000(7)	0.0117	0.0111(9)	0.0113(9)	0.0131(10)	0.0000	0.0036(8)	0.0000

Note: Standard deviations are in parentheses.

shortening of all T-O individual distances except T-O3. On the contrary, the M1 and M2 octahedra (Figs. 3b and 3c) expand almost linearly up to 673 K, the evolution of M1 volume with temperature being more scattered than M2. The thicknesses of the interlayer and of the octahedral sheet as a function of temperature are reported in Figure 4. While the mean tetrahedral thickness remains essentially unchanged over the temperature range 100–673 K (see Table 7), the octahedral sheet thickens by 0.02 Å, and the interlayer expands from 3.384 to 3.451 Å in the same range. Therefore the thermal expansion along the **c**-axis is mainly due to the dilation of the interlayer. As concerns the intercalated K^+ cation, the mean distance <K-O> increases slightly with temperature, thus the polyhedron around the interlayer cation expands, as evident from Figure 5. It is worth noting that the shorter cation-oxygen distances $<K\text{-}O>_{inner}$ increase, whereas the longer ones, $<K\text{-}O>_{outer}$, decrease about in the same proportion. As already observed by McCauley and Newnham (1971), the difference between inner and outer K-O distances (Δk) is linearly related to the ditrigonal distortion, and produces a more regular arrangement of the site as the temperature increases.

At 873 and 1023 K, concomitant with the decrease in lattice parameters, most of the structural parameters considered above show sharp discontinuities, which may be summarized as follows: (1) abrupt changes of T-O3 and M1-O bond distances (see data in Table 6); (2) tetrahedral volume and thickness exhibit an irregular trend of expansion at 873 K (point a in Fig. 3a), followed by a contraction in the subsequent data collection at the same temperature (point b in Fig. 3a), and again an expansion at 1023 K. Octahedral sheet and interlayer thicknesses display an opposite behavior (Fig. 4), while octahedral volumes (Figs. 3b and 3c), substantially constant at 873 K (points a and b), undergo a contraction at 1023 K. This contraction is mostly a consequence of the strong shortenings of M-O4 bond lengths at 873 K (Fig. 6), which become more pronounced at 1023 K.

These structural changes turn out to be irreversible as shown by the reversal experiment. Indeed, from the results of the structure refinement of data collected at 298 K after the heating cycle, we observe a reduction in the unit-cell dimensions with respect

TABLE 5B. Crystallographic coordinates, occupancies, and equivalent isotropic displacement parameters (Å²)

Atom	*x*	*y*	*z*	Occupancy	$U_{iso/equiv}$
473 K					
K	0.0000	0.5000	0.0000	1.0291(8)	0.0459(14)
M1(Mg)	0.0000	0.0000	0.5000	0.7399(7)	0.0126(10)
M1(Fe)	0.0000	0.0000	0.5000	0.2601(7)	0.0126(10)
M2(Mg)	0.0000	0.3350(3)	0.5000	0.7380(7)	0.0138(7)
M2(Fe)	0.0000	0.3350(3)	0.5000	0.2620(7)	0.0138(7)
Si	0.0756(4)	0.1668(2)	0.2261(2)	0.9799(9)	0.0128(6)
O1	0.3254(12)	0.2314(7)	0.1680(6)	1.0000(8)	0.0269(16)
O2	0.0157(16)	0.0000	0.1705(9)	1.0000(8)	0.022(2)
O3	0.1311(10)	0.1676(7)	0.3916(6)	1.0000(8)	0.0149(13)
O4	0.1275(16)	0.5000	0.3974(9)	1.0000(8)	0.0179(19)
673 K					
K	0.0000	0.5000	0.0000	1.0279(8)	0.058(2)
M1(Mg)	0.0000	0.0000	0.5000	0.7397(7)	0.0172(14)
M1(Fe)	0.0000	0.0000	0.5000	0.2603(7)	0.0172(14)
M2(Mg)	0.0000	0.3352(4)	0.5000	0.7380(7)	0.0190(10)
M2(Fe)	0.0000	0.3352(4)	0.5000	0.2620(7)	0.0190(10)
Si	0.0755(5)	0.1668(3)	0.2268(3)	0.9800(9)	0.0164(8)
O1	0.3188(15)	0.2356(10)	0.1697(8)	1.0000(8)	0.034(2)
O2	0.028(2)	0.0000	0.1721(13)	1.0000(8)	0.037(3)
O3	0.1315(13)	0.1672(8)	0.3919(7)	1.0000(8)	0.0208(17)
O4	0.128(2)	0.5000	0.3976(11)	1.0000(8)	0.023(3)
873 K					
K	0.0000	0.5000	0.0000	1.0331(9)	0.079(3)
M1(Mg)	0.0000	0.0000	0.5000	0.7383(8)	0.0218(17)
M1(Fe)	0.0000	0.0000	0.5000	0.2617(8)	0.0218(17)
M2(Mg)	0.0000	0.3364(5)	0.5000	0.7378(8)	0.0229(13)
M2(Fe)	0.0000	0.3364(5)	0.5000	0.2622(8)	0.0229(13)
Si	0.0761(6)	0.1668(4)	0.2277(4)	0.9802(9)	0.0198(11)
O1	0.317(2)	0.2415(12)	0.1679(10)	1.0000(7)	0.038(3)
O2	0.038(3)	0.0000	0.1720(14)	1.0000(7)	0.036(4)
O3	0.1308(16)	0.1682(11)	0.3918(9)	1.0000(7)	0.025(2)
O4	0.131(2)	0.5000	0.3992(13)	1.0000(8)	0.024(3)
873 K*					
K	0.0000	0.5000	0.0000	1.0277(8)	0.077(3)
M1(Mg)	0.0000	0.0000	0.5000	0.7395(7)	0.0228(16)
M1(Fe)	0.0000	0.0000	0.5000	0.2605(7)	0.0228(16)
M2(Mg)	0.0000	0.3375(5)	0.5000	0.7379(7)	0.0214(12)
M2(Fe)	0.0000	0.3375(5)	0.5000	0.2621(7)	0.0214(12)
Si	0.0760(6)	0.1670(4)	0.2272(3)	0.9801(9)	0.0195(10)
O1	0.3168(18)	0.2400(11)	0.1696(10)	1.0000(8)	0.038(2)
O2	0.038(3)	0.0000	0.1710(15)	1.0000(8)	0.039(4)
O3	0.1308(15)	0.1686(10)	0.3900(8)	1.0000(8)	0.023(2)
O4	0.133(2)	0.5000	0.3995(12)	1.0000(8)	0.028(3)
1023 K					
K	0.0000	0.5000	0.0000	1.0351(9)	0.086(3)
M1(Mg)	0.0000	0.0000	0.5000	0.7377(8)	0.0297(17)
M1(Fe)	0.0000	0.0000	0.5000	0.2623(8)	0.0297(17)
M2(Mg)	0.0000	0.3405(5)	0.5000	0.7381(8)	0.0245(11)
M2(Fe)	0.0000	0.3405(5)	0.5000	0.2619(8)	0.0245(11)
Si	0.0749(6)	0.1674(3)	0.2268(3)	0.9796(9)	0.0217(9)
O1	0.3132(17)	0.2425(10)	0.1683(8)	1.0000(7)	0.038(2)
O2	0.041(3)	0.0000	0.1718(12)	1.0000(7)	0.042(3)
O3	0.1315(14)	0.1688(9)	0.3916(7)	1.0000(7)	0.0268(19)
O4	0.134(2)	0.5000	0.4012(12)	1.0000(8)	0.028(3)

Note: Standard deviations are in parentheses.
* After 14 h from previous measurement at the same temperature.

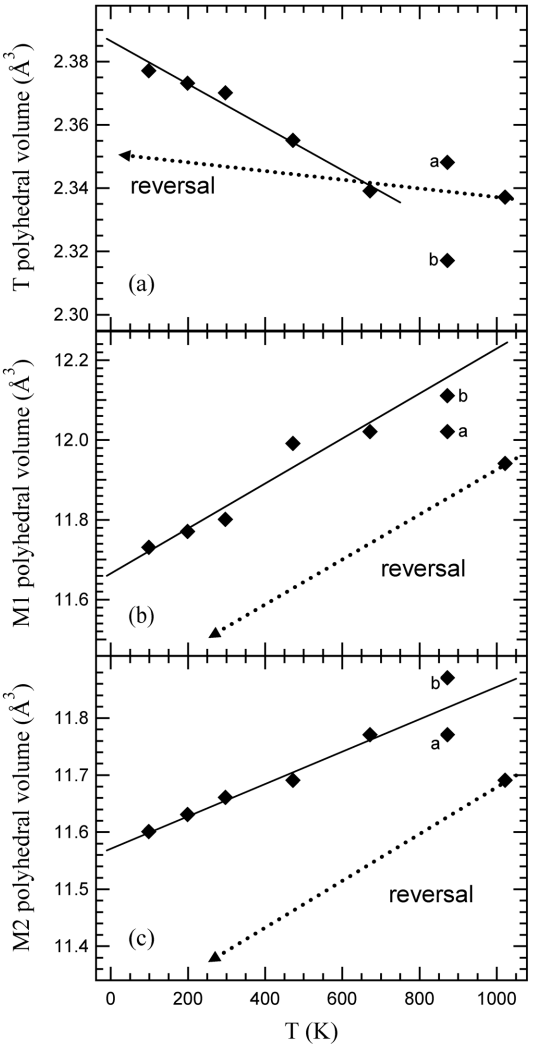

FIGURE 3. Polyhedral volumes as a function of temperature. Linear regressions across 100–673 K temperature range are reported. Subsequent structural investigations at 873 K are marked with a and b labels. Dashed arrows indicate reversal experiment. (**a**) T site; (**b**) M1 site; (**c**) M2 site.

to the unheated sample (see Table 3). In addition, the octahedral sheet thickness reduces from 2.133 to 2.106 Å, and both M1 and M2 polyhedra contract. Mean bond distances <M1-O> and <M2-O> decrease, mainly owing to the strong shortening of M-O4 distances (see Tables 6 and 7). Tetrahedral sheet thickness remains unchanged, while both tetrahedral cation-basal O atoms bond distances and volume decrease. The mean <K-O> distance shortens in spite of a little increase of $<K\text{-}O>_{inner}$ bond lengths. Taking into account the Mossbauer data, it is apparent that all Fe^{2+} was transformed into Fe^{3+} after annealing at $T = 900$ K. This transformation also reflects the structural features of SA sample observed at 873, 1023, and 298 K after the heating treatment, which clearly indicate the occurrence of an irreversible Fe^{2+} oxidation balanced by a loss of H_2 at the O4 site.

DISCUSSION

In situ structural investigation of trioctahedral mica SA in the temperature range 100–1023 K showed the occurrence of a deprotonation process with consequent $Fe^{2+} \rightarrow Fe^{3+}$ oxidation starting from 873 K. This process is irreversible under the conditions of the present study and can be described by the following reaction:

$$Fe^{2+} + OH^- \rightarrow Fe^{3+} + O^{2-} + H\uparrow \quad (1)$$

This hypothesis is validated by the results of Mössbauer spectroscopy as well as by structural considerations. The curve

TABLE 6. Selected bond distances (Å) for SA sample at different temperature (K)

	100 K	200 K	298 K	473 K	673 K	873 K	873 K*	1023 K	298 K†
Tetrahedral sheet									
T-O1	1.6660(7)	1.6647(7)	1.6641(8)	1.664(6)	1.648(8)	1.675(10)	1.655(9)	1.657(8)	1.6533(19)
T-O1′	1.6657(7)	1.6649(8)	1.6636(8)	1.658(6)	1.664(9)	1.653(11)	1.654(10)	1.654(9)	1.658(2)
T-O2	1.6650(5)	1.6638(5)	1.6638(5)	1.656(4)	1.650(5)	1.652(6)	1.654(6)	1.653(5)	1.6567(13)
T-O3	1.6704(7)	1.6708(7)	1.6697(7)	1.671(6)	1.671(8)	1.663(10)	1.649(9)	1.669(8)	1.673(2)
<T-O>	1.6668	1.6661	1.6653	1.662	1.658	1.661	1.653	1.658	1.660
Octahedral sheet									
M1-O4 ×2	2.0514(9)	2.0530(9)	2.0545(10)	2.082(8)	2.083(11)	2.066(13)	2.056(13)	2.046(11)	2.025(2)
M1-O3 ×4	2.0909(6)	2.0916(7)	2.0936(6)	2.097(6)	2.099(7)	2.108(9)	2.120(8)	2.113(8)	2.0873(17)
<M1-O>	2.0777	2.0787	2.0806	2.092	2.094	2.094	2.099	2.091	2.067
M2-O4 ×2	2.0311(6)	2.0322(7)	2.0351(7)	2.036(6)	2.041(8)	2.033(10)	2.026(9)	1.998(8)	1.980019)
M2-O3 ×2	2.0921(7)	2.0935(7)	2.0956(7)	2.096(6)	2.104(9)	2.108(10)	2.122(9)	2.133(9)	2.0796(16)
M2-O3′×2	2.0831(6)	2.0839(7)	2.0861(7)	2.086(5)	2.088(7)	2.094(9)	2.101(8)	2.094(8)	2.1151(17)
<M2-O>	2.0688	2.0699	2.0723	2.073	2.078	2.078	2.083	2.075	2.058
<M-O>	2.0718	2.0728	2.0751	2.079	2.083	2.083	2.088	2.080	2.061
Interlayer									
K-O1 ×4	2.916(1)	2.931(1)	2.951(1)	2.996(9)	3.057(8)	3.094(10)	3.092(9)	3.109(9)	2.928(2)
K-O1′×4	3.398(1)	3.391(1)	3.382(1)	3.333(7)	3.305(9)	3.257(11)	3.273(10)	3.243(9)	3.352(2)
K-O2 ×2	2.918(1)	2.934(1)	2.953(1)	2.993(9)	3.062(13)	3.108(15)	3.104(15)	3.122(13)	2.935(3)
K-O2′×2	3.407(1)	3.400(1)	3.389(1)	3.365(8)	3.326(12)	3.286(14)	3.276(14)	3.268(12)	3.361(3)
<K-O_{inner}>	2.917	2.932	2.952	2.995	3.059	3.099	3.096	3.113	2.930
<K-O_{outer}>	3.401	3.394	3.384	3.344	3.312	3.267	3.274	3.251	3.355
<K-O>	3.159	3.163	3.168	3.170	3.186	3.183	3.185	3.182	3.143

Note: Standard deviations are in parentheses.
* 14 h after previous measurement at the same temperature.
† Sample after heating cycle.

TABLE 7. Geometric parameters derived from the structure refinements in space group *C*2/*m* at different temperatures (K)

T (K)	100	200	298	473	673	873	873*	1023	298†
t_{tet} (Å)	2.244	2.243	2.243	2.249	2.241	2.256	2.227	2.250	2.245
BLD_T	0.142	0.147	0.131	0.326	0.562	0.501	0.127	0.333	0.369
Volume T (Å^3)	2.377	2.373	2.370	2.355	2.339	2.348	2.317	2.337	2.347
TQE	1.0001	1.0002	1.0002	1.0004	1.0003	1.0008	1.0003	1.0005	1.0002
TAV	0.463	0.517	0.584	1.241	0.630	2.7020	1.241	1.500	0.676
τ (°)	110.09	110.12	110.17	110.40	110.15	110.91	110.47	110.55	110.22
α (°)	10.58	10.10	9.47	7.65	5.59	3.69	3.91	3.03	9.28
ECoN	9.41	9.65	9.96	10.69	11.35	11.70	11.72	11.11	10.00
Δ*z* (Å)	0.009	0.0101	0.0081	0.0252	0.0243	0.0416	0.0142	0.0354	0.014
D.M. (Å)	0.597	0.582	0.568	0.510	0.478	0.463	0.440	0.468	0.579
Ψ_{M1} (°)	59.10	59.10	59.13	59.08	59.12	59.22	58.96	59.37	59.36
Ψ_{M2} (°)	58.96	58.95	58.98	58.78	58.85	58.96	58.71	59.11	59.22
BLD_{M1}	0.820	0.831	0.843	0.382	0.343	0.902	1.366	1.432	1.343
ELD_{M1}	5.243	5.241	5.269	5.216	5.257	5.374	5.081	5.552	5.544
BLD_{M2}	1.195	1.207	1.200	1.176	1.189	1.459	1.819	2.474	2.542
ELD_{M2}	5.073	5.061	5.097	4.862	4.947	5.069	4.775	5.235	5.364
$Shift_{M2}$ (Å)	0.017	0.017	0.017	0.015	0.017	0.029	0.039	0.067	0.073
Volume M1 (Å)	11.73	11.77	11.80	11.99	12.02	12.02	12.11	11.94	11.53
OQE_{M1}	1.0122	1.0122	1.0124	1.0120	1.0122	1.013	1.0117	1.0141	1.0140
OAV_{M1}	39.349	39.677	39.831	39.094	39.885	41.500	37.259	44.399	44.071
Volume M2 (Å^3)	11.60	11.63	11.66	11.69	11.77	11.77	11.87	11.69	11.39
OQE_{M2}	1.0115	1.0115	1.0116	1.0105	1.0109	1.0117	1.0107	1.0135	1.0143
OAV_{M2}	37.154	37.361	37.723	34.061	35.477	37.689	34.199	42.156	44.681
t_{oct} (Å)	2.133	2.135	2.136	2.149	2.150	2.144	2.164	2.131	2.106
t_{int} (Å)	3.384	3.395	3.405	3.410	3.451	3.432	3.445	3.432	3.348
$t_{K\text{-}O4}$ (Å)	3.947	3.953	3.958	3.951	3.962	3.985	3.984	4.001	3.945

Notes: t_{tet} = tetrahedral sheet thickness calculated from the *z* coordinates of basal and apical O atoms; TQE = tetrahedral quadratic elongation (Robinson et al. 1971); TAV = tetrahedral angle variance (Robinson et al. 1971); τ = tetrahedral flattening angle; α = tetrahedral rotation angle (Hazen and Burnham 1973); Δ*z* = departure from co-planarity of the basal O atoms (Güven 1971); D.M. = dimensional misfit between tetrahedral and octahedral sheets (Toraya 1981); ψ = octahedral flattening angles (Donnay et al. 1964a, 1964b); BLD = bond-length distortions (Renner and Lehmann 1986); ELD = edge-length distortion (Renner and Lehman 1986); $Shift_{M2}$ = off-center shift of the M2 cation defined as the distance between the refined position of cation and the geometrical center of M2 site (coordinates: *x*/*a* = 0.0, *y*/*b* = 0.8333, *z*/*c* = 0.5); OQE = octahedral quadratic elongation (Robinson et al. 1971); OAV = octahedral angle variance (Robinson et al. 1971); t_{oct} = octahedral sheet thickness (Toraya 1981); t_{int} calculated from the *z* coordinates of basal O atoms; $t_{K\text{-}O4}$ = projection of K-O4 distance along **c***; ECoN = effective coordination number (Nespolo et al. 2001).
* 14 h after previous measurement at the same temperature.
† Sample after heating cycle.

through the points up to 823 K is therefore assumed to represent sample expansion prior to the deprotonation reaction, as well as reversal experiment represents thermal expansion of the corresponding Fe^{3+}-bearing sample. Axial thermal expansion is linear both in the sample prior to the deprotonation process and after $Fe^{2+} \rightarrow Fe^{3+}$ oxidation and, as expected for a 2D layer structure, is more pronounced along the **c**-axis.

It is worth noting that the discontinuity in the variations of the unit-cell parameters is clear evidence of the occurrence of a phase transition implying no symmetry change, as proven by the

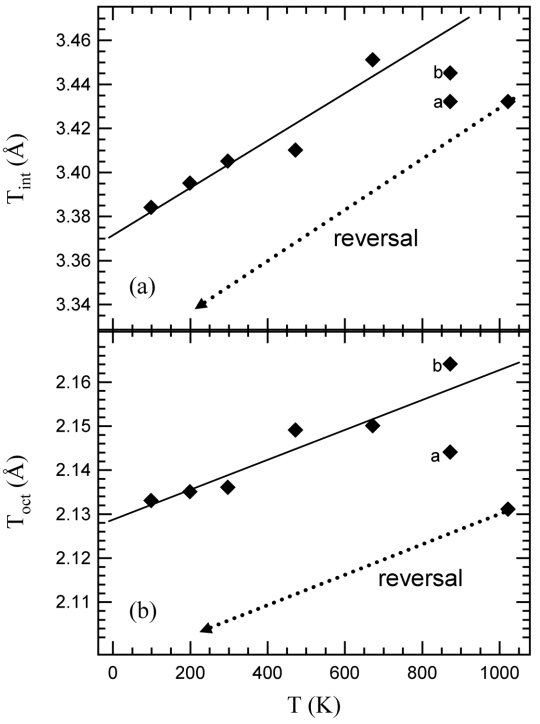

FIGURE 4. Thicknesses of (**a**) interlayer and (**b**) octahedral sheet vs. temperature. Linear regressions across 100–673 K are reported. Subsequent structural investigations at 873 K are marked with a and b labels. Dashed arrows indicate reversal experiment.

TABLE 8. Mean atomic numbers of cation sites and octahedral and tetrahedral mean distances as determined by structure refinement at RT and chemical analyses (EMPA)

	SA	SA*
$e^-_{(M1)\ X\text{-}ref}$	15.67	15.65
$e^-_{(M2)\ X\text{-}ref}$	15.74	15.67
$e^-_{(M1+M2)\ X\text{-}ref}$	47.15	46.99
$e^-_{(M1+M2)\ EMPA}$	47.34	47.34
$K\ e^-_{X\text{-}ref}$	19.48	19.41
$K\ e^-_{EMPA}$	19.04	19.04
$T\ e^-_{X\text{-}ref}$	13.73	13.71
$T\ e^-_{EMPA}$	13.69	13.69
Σ^+	22.67	22.96
Σ^-	22.66	22.95
$\langle T\text{-}O\rangle_{X\text{-}ref}$	1.665	1.660
$\langle T\text{-}O\rangle_{EMPA}$	1.666	1.661
$\langle M\text{-}O\rangle_{X\text{-}ref}$	2.075	2.061
$\langle M\text{-}O\rangle_{EMPA}$	2.068	2.074

* Sample after heating cycle.

structure refinement of data collected at 1023 K. The Fe^{3+}-bearing phase obtained at $T \geq 873$ K is in fact stable, as evidenced by the irreversibility of the process, and is characterized by slightly different physical properties, e.g., by a more pronounced anisotropy of the thermal expansion behavior.

Axial thermal expansion coefficients obtained in this study on sample SA during "heating up" and "cooling down" experiments are compared in Table 9 with data on other trioctahedral micas taken from the literature in almost the same range of temperature. The observed trends are in good agreement with those of micas with similar composition. The lower values of α_a and α_b

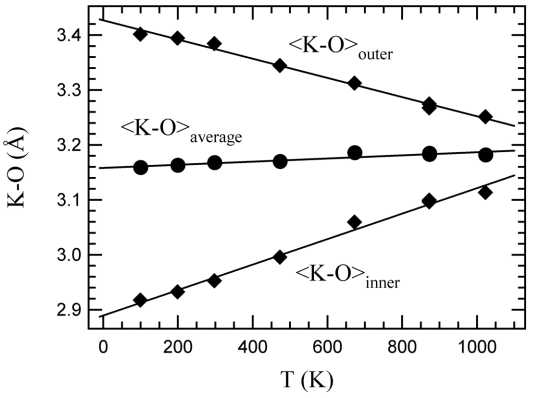

FIGURE 5. Variation of mean $\langle K\text{-}O\rangle_{inner}$, $\langle K\text{-}O\rangle_{outer}$, and $\langle K\text{-}O\rangle$ distances with temperature.

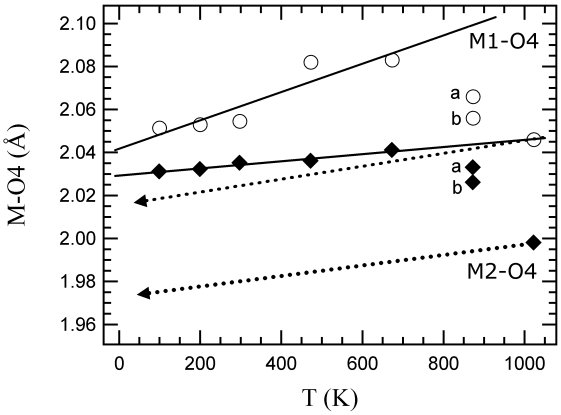

FIGURE 6. Plot of M1-O4 (circles) and M2-O4 (diamonds) bond distances as a function of temperature. Linear regressions across 100–673 K temperature range are reported. Subsequent structural investigations at 873 K are marked with a and b labels. Dashed arrows indicate reversal experiment.

measured during the reversal experiment can be attributed to the variation of octahedral composition because of Fe^{2+}/Fe^{3+} oxidation. The differences in the expansivities over the temperature range 100–823 K can be ascribed to differences in chemical composition. Coulombic interaction between anionic content at site O4 and interlayer cation greatly determines **c**-axis expansion, while composition of octahedral sites influences expansion along the **a-** and **b**-axis. This feature had been already evidenced in axial expansion of synthetic Cs-tetra-ferriannite (Comodi et al. 1999). Previous studies on a fluorophlogopite (Takeda and Morosin 1975) and a F-rich phlogopite (Tutti et al. 2000) showed two expansivity rates below and above 400 °C, due to different Mg octahedral expansion mode. In this study no significant deviation from the linear expansion of cell parameters in the temperature range 100–823 K was observed within experimental uncertainty. The discontinuity observed at 873 K is in clear agreement with the break in the expansion rate reported by Chon et al. (2006) and by Russell and Guggenheim (1999), and interpreted as due to the Fe oxidation and deprotonation processes.

The expansion along the **c**-axis is dominated by the interlayer dilation. The octahedral sheet has only a small effect, while the

TABLE 9. Comparison between thermal expansion coefficients ($\times 10^{-5}$/K) of trioctahedral micas reported in the literature

Crystal-chemical formula	α_a	α_b	α_c	α_V	*T* range (K)	Ref
$KMg_3Si_3AlO_{10}F_2$	0.98	0.93	1.73	3.91	298–623	1
	0.62	0.48	1.70	3.06	673–1073	1
$(K_{0.82}Na_{0.115})(Mg_{2.28}Fe^{2+}_{0.12}Al_{0.495}\square_{0.105})(Si_{2.785}Al_{1.215})O_{10.00}(OH_{1.932}F_{0.068})$	1.40	1.35	1.81	4.66	298–873	2
$Cs_{0.98}Fe^{2+}_{2.965}Fe^{3+}_{0.035}Si_{3.075}Al_{0.025}Fe^{3+}_{0.9}O_{10}OH_2$	–	–	3.12	–	298–873	3
$(K_{0.869}Na_{0.08})(Mg_{2.832}Ti_{0.001}Fe^{2+}_{0.121}Al_{0.045}Mn_{0.002})(Si_{3.009}Al_{0.991})O_{10}(OH_{0.644}F_{1.356})$	3.74	1.09	1.19	6.26	298–623	4
	0.86	0.80	1.93	3.71	685–1073	4
$(K_{0.98}Na_{0.065})(Mg_{1.58}Ti_{0.085}Fe^{2+}_{1.3}Mn_{0.045})(Si_{2.99}Al_{0.96}Ti_{0.05})O_{10}(OH_{0.735}F_{0.99})$	0.44	0.52	1.65	2.71	298–873	5
$(K)(Mg_{2.23}Fe_{0.425}Ti_{0.11})(Si_{2.755}Al_{1.245})O_{10.00}(OH_{1.795}F_{0.205})$	1.14	1.12	1.71	–	298–773	6
	0.71	0.61	1.62	–	773–1073	6
$(K_{0.85}Na_{0.11}Ba_{0.03})(Mg_{1.98}Al_{0.17}Mn_{0.01}Fe^{2+}_{0.29}Fe^{3+}_{0.37}Ti_{0.18})(Si_{2.75}Al_{1.25})O_{10.66}(OH_{1.20}F_{0.13}Cl_{0.01})$	1.24(4)	1.40(4)	1.47(4)	4.10(4)	298–823	7
$(K_{0.85}Na_{0.11}Ba_{0.03})(Mg_{1.98}Al_{0.17}Mn_{0.01}Fe^{3+}_{0.66}Ti_{0.18})(Si_{2.75}Al_{1.25})O_{10.95}(OH_{0.91}F_{0.13}Cl_{0.01})$	1.11(2)	1.16(3)	1.71(4)	4.03(2)	298–1023*	7

Notes: 1 = Takeda and Morosin (1975); 2 = Russell and Guggenheim (1999); 3 = Comodi et al. (1999); 4 = Tutti et al. (2000); 5 = Chon et al. (2003); 6 = Chon et al. (2006); 7 = this work.
* Under reversal conditions.

tetrahedral sheet contribution is nil up to 673 K, and slightly negative after 673 K. Energy minimization due to microscopic displacements (inner strain) (Catti 1985; Mookherjee and Redfern 2002) of the basal O atoms explains the larger interlayer thickness expansivity with respect to the whole dilation along the **c*** direction. As already stated, the K-polyhedron expands and becomes more regular as temperature increases; the effective coordination number (ECoN), calculated through the iterative procedure described in Nespolo et al. (2001), increases from 9.4 to 11.3 as temperature rises from 100 to 673 K. The expansion of the upper and lower oxygen triads, forming the interlayer polyhedron, is greater than the interlayer separation. This induces an increasing of the flattening angle of the K site, which evolves from a polyhedron elongated in the **c** direction to a flattened polyhedron as temperature increases. Similar behavior was found in thermal expansions of phlogopite end-member mica (Russell and Guggenheim 1999) and of Fe-rich, F-rich phlogopite (Takeda and Morosin 1975; Russell and Guggenheim 1999). Substitutions of Fe for Mg and F for OH determine a more flattened K-polyhedron.

The octahedral sheet expands laterally reducing the misfit with the tetrahedral sheet. The adjustment of the T-O-T layer is accomplished by a slight compression of tetrahedral volume, and more by in-plane rotations of the tetrahedra. The rotation angle, α, decreases with increasing temperature from 10.58° (at 100 K) to 3.58 (at 873 K). According to the geometric model of Brigatti and Guggenheim (2002), α is strongly related to $\langle O\text{-}O\rangle_u$, unshared octahedral edges, and $\langle O\text{-}O\rangle_b$, tetrahedral basal edges, through the following relation: $\alpha = \arccos[(3/4)^{1/2}k]$, where $k = \langle O\text{-}O\rangle_u/\langle O\text{-}O\rangle_b$. Note that α decreases as $\langle O\text{-}O\rangle_u$ increases and $\langle O\text{-}O\rangle_b$ decreases. Therefore the α decrease is correlated to the tetrahedral contraction and octahedral expansion. As a consequence the silicate ring tends to become more regular as temperature increases.

M1 and M2 octahedra are flattened and expand with temperature essentially fixed in shape. The tetrahedron is fairly regular and slightly elongated along the T-O_{apical} bond distance (O_{basal}-T-O_{apical} = 110.89°, O_{basal}-T-O_{basal} = 108.23° at T = 298 K). The tetrahedral bond lengths T-O1 and T-O2 are quite homogeneous in the range 100–298 K. The T-O individual distances decrease over this T range, and above all at 873 K. It is an apparent shortening of tetrahedral bond distances with temperature, without counting the effects of thermal motion (Downs et al. 1992).

All the sharp structural changes observed at 873 K can be explained on the basis of the deprotonation/oxidation process: (1) remarkable shortening of M-O4 bond lengths (see Table 6); (2) high $shift_{M2}$ value (see Table 7); and (3) notable shortening of O4-O4 edge shared by two adjacent M2 sites (from 2.696 Å at 100 K to 2.684 Å at 1023 K). These effects are more marked at 1023 K, and are associated with octahedral and interlayer thicknesses compression. The strong displacement of M2 cation toward the hydroxyl site (O4) is ascribed to the increase of Coulombic attraction due to the following local changes $Fe^{2+} \rightarrow Fe^{3+}$ and $OH^- \rightarrow O^{2-}$. The shortening of O4-O4 edge provides a better screening to the increased repulsion between adjacent M2 cations. Octahedral thickness compression is due to change in cation size from Fe^{2+} to Fe^{3+}, while interlayer thickness variation is due to the loss of H_2 that reduces the repulsive interaction K^+-H^+. Similar trends had been already found in earlier works (Russell and Guggenheim 1999; Chon et al. 2006). Nevertheless some of the structural features observed in this work differ in magnitude, mostly because of the different amount of Fe^{2+} involved in the dehydrogenation mechanism, and of the experimental conditions (particle size, process environment) that determine temperature and extent of the oxy mechanism.

The room-temperature structure refinement of crystal SA after heating indicates a reduction in tetrahedral and octahedral thicknesses with respect to the same sample before thermal treatment. T-O1 and T-O2 individual distances are shortened, while T-O3 apical bond distance remains unchanged; as a consequence the tetrahedron becomes more distorted (see BLD, TAV, and τ in Table 7). Both the M-octahedra reduce greatly their volumes by the same extent, changing their shape [higher values of Ψ(M1,M2)] especially as far as M2 is concerned. M-O4 distances are strongly reduced, while the M2-O3 bond length is increased. In addition, the separation and volume interlayer in the heat-treated sample are decreased with respect to that one of the untreated sample.

All these structural modifications are attributed, in agreement with previous studies (Ohta et al. 1982; Comodi et al. 1999; Russell and Guggenheim 1999), to the occurrence of the oxidation-deprotonation process described above. Moreover, structural data suggest that the oxidation of divalent iron takes place in both the M1 and M2 sites, in analogy with what reported by Russell and Guggenheim (1999), who showed that in a Fe-rich phlogopite both M1-O and M2-O mean distances shorten after heating. On the other hand, Comodi et al. (1999) observed that, unlike the M2 *cis* octahedron, heating did not affect significantly the M1

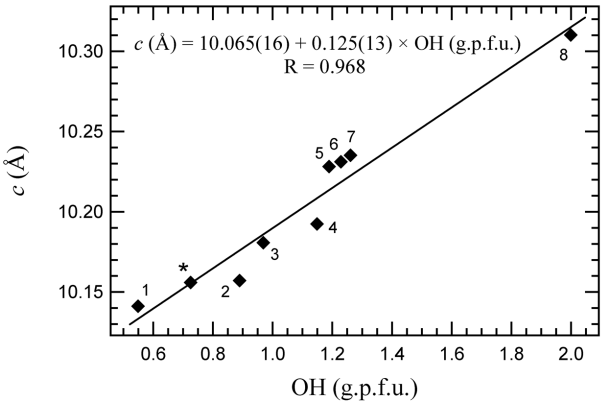

FIGURE 7. Plot of *c* cell parameter vs. OH content in groups per formula unit (gpfu). Solid line represents regression analysis on following data: (1) VUT 215_5 (Matarrese et al. 2008); (2) VUT191_19 (Matarrese et al. 2008); (3) VUT191_11 (Matarrese et al. 2008); (4) VUT191_10 (Matarrese et al. 2008); (5) VUT187_24 (Schingaro personal communication); (6) SA1_52 (Scordari et al. 2006); (7) VUT187_31 (Schingaro personal communication); and (8) Phl2 (Redhammer and Roth 2002). Estimated OH content of sample SA after heating is given by point *.

trans octahedron, in fact the M1-O mean distance as well as the polyhedral volume remained substantially unchanged. On the basis of this geometrical feature and other structural evidences they argued that the oxidation of Fe^{2+} in synthetic Cs-tetraferriannite occurs mainly at the M2 site.

Discontinuities observed at 873 and 1023 K are ascribed to events of the same oxidation-deprotonation process. Under the experimental conditions of the present study it is not possible to assess whether these marked events are separate or part of a reaction over the range 873–1023 K. However, according to findings from previous studies (Tutti et al. 2000; Chon et al. 2006), the second hypothesis seems more likely. As concerns the heated sample, in absence of a direct H determination after the heating cycle, the crystal chemical formula (see Mössbauer section) could be in question. However, a semiquantitative estimation of OH content can be deduced from the **c** parameter vs. OH content relationship, reported in Figure 7. The value (0.73 groups per formula unit) obtained from a linear regression using samples with similar chemistry and with known OH content is in good agreement with the one reported.

Finally, we observe that the results of this research are in agreement with the structural formulae and the cation partitioning proposed by Scordari et al. (2006). Those authors deduced from geometrical data and refined mean atomic numbers the probable population of M1 and M2 sites, which resulted in an almost equal distribution of Fe^{2+} over the octahedral sites.

ACKNOWLEDGMENTS

The authors are grateful to Marcello Serracino for assistance during electron probe microanalyses at the Istituto di Geologia Ambientale e Geoingegneria, CNR, Rome. We thank M. Rieder, G. Ferraris, and the Associate Editor, W. Huff, for their remarks and suggestions that allowed to improve appreciably the manuscript. This work was supported by the COFIN-MIUR (2006).

REFERENCES CITED

Betteridge, P.W., Carruthers, J.R., Cooper, R.I., Prout, K., and Watkin, D.J. (2003) Crystals version 12: Software for guided crystal structure analysis. Journal of Applied Crystallography, 36, 1487.

Blessing, R.H. (1995) An empirical correction for absorption anisotropy. Acta Crystallographica, A51, 33–38.

Blessing, R.H., Coppens, P., and Becker, P. (1974) Computer analysis of step scanned X-ray data. Journal of Applied Crystallography, 7, 488–492.

Brigatti, M.F. and Guggenheim, S. (2002) Mica crystal chemistry and the influence of pressure, temperature, and solid solution on atomistic models. In A. Mottana, F.P. Sassi, J.B. Thompson, and S. Guggenheim, Eds., Micas: Crystal Chemistry and Metamorphic Petrology, 46, p. 1–100. Reviews in Mineralogy and Geochemistry, Mineralogical Society of America, Chantilly, Virginia.

Bruker (2001) SAINT. Bruker AXS Inc., Madison, Wisconsin, U.S.A.

——— (2003) APEX2. Bruker AXS Inc., Madison, Wisconsin, U.S.A.

Catti, M. (1985) Calculation of elastic constants by the method of crystal static deformation. Acta Crystallographica, A41, 494–500.

Chon, C-M., Kim, S.A., and Moon, H-S. (2003) Crystal structures of biotite at high temperatures and of heat-treated biotite using neutron powder diffraction. Clays and Clay Minerals, 51, 519–528.

Chon, C-M., Lee, C-K., Song, Y., and Kim, S.A. (2006) Structural changes and oxidation of ferroan phlogopite with increasing temperature: In situ neutron neutron powder diffraction and Fourier transform infrared spectroscopy. Physics and Chemistry of Minerals, 33, 289–299.

Comodi, P., Zanazzi, P.F., Weiss, Z., Rieder, M., and Drábek, M. (1999) "Cs-tetraferri-annite:" High-pressure and high-temperature behavior of a potential nuclear waste disposal phase. American Mineralogist, 84, 325–332.

Donnay, G., Morimoto, N., Takeda, H., and Donnay, J.D.H. (1964a) Trioctahedral one-layer micas. I. Crystal structure of a synthetic iron mica. Acta Crystallographica, 17, 1369–1373.

Donnay, G., Donnay, J.D.H., and Takeda, H. (1964b) Trioctahedral one-layer micas. II. Prediction of the structure from composition and cell dimensions. Acta Crystallographica, 17, 1374–1381.

Downs, R.T., Gibbs, G.V., Bartelmehs, K.L., and Boisen, M.B. Jr. (1992) Variations of bond lengths and volumes of silicate tetrahedra with temperature. American Mineralogist, 77, 751–757.

Dyar, M.D. (2002) Optical and Mössbauer spectroscopy of iron in micas. In A. Mottana, F.P. Sassi, J.B. Thompson, and S. Guggenheim, Eds., Micas: Crystal Chemistry and Metamorphic Petrology, 46, p. 313–340. Reviews in Mineralogy and Geochemistry, Mineralogical Society of America, Chantilly, Virginia.

Güven, N. (1971) The crystal structure of $2M_1$ phengite and $2M_1$ muscovite. Zeitschrift für Kristallographie, 134, 196–212.

Hawthorne, F.C., Ungaretti, L., and Oberti, R. (1995) Site populations in minerals: Terminology and presentation of results. Canadian Mineralogist, 33, 907–911.

Hazen, R.M. and Burnham, C.W. (1973) The crystal structure of one layer phlogopite and annite. American Mineralogist, 58, 889–900.

Kogarko, L.N., Uvarova, Y.A., Sokolova, E., Hawthorne, F.C., Ottolini, L., and Grice, J.D. (2005) Oxykinoshitalite, a new mica from Fernando-de-Norohna Island, Brazil: occurrence and crystal structure. Canadian Mineralogist, 43, 1501–1510.

Lagarec, K. and Rancourt, D.G. (1998) RECOIL. Mössbauer spectral analysis software. University of Ottawa, Canada (http://www.isapps.ca/recoil).

Lehman, M.S. and Larsen, F.K. (1974) A method for location of the peaks in step-scan measured Bragg reflections. Acta Crystallographica, A30, 580–584.

Matarrese, S., Schingaro, E., Scordari, F., Stoppa, F., Rosatelli, G., Pedrazzi, G., and Ottolini, L. (2008) Crystal chemistry of phlogopite from Vulture-S. Michele subsynthem volcanics (Mt. Vulture, Italy) and volcanological implications. American Mineralogist, 93, 426–437.

McCauley, J.W. and Newnham, R.E. (1971) Origin and prediction of ditrigonal distorsions in micas. American Mineralogist, 56, 1626–1638.

Mookherjee, M. and Redfern, S.A.T. (2002) A high-temperature Fourier transform infrared study of the interlayer and Si-O-stretching region in phengite-$2M_1$. Clay Minerals, 37, 323–336.

Nespolo, M., Ferraris, G., Ivaldi, G., and Hoppe, R. (2001) Charge distribution as a tool to investigate structural details. II. Extension to hydrogen bonds, distorted and hetero-ligand polyhedra. Acta Crystallographica, B57, 652–664.

North, A.C.T., Phillips, D.C., and Mathews, F.S. (1968) A semi-empirical method of absorption correction. Acta Crystallographica, A24, 351–359.

Ohta, T., Takeda, H., and Takéuchi, Y. (1982) Mica polytypism: Similarities in the crystal structures of coexisting $1M$ and $2M_1$ oxybiotite. American Mineralogist, 67, 298–310.

Pouchou, J-L. and Pichoir, F. (1985) 'PAP' Φ(ρZ) procedure for improved quantitative micro-analysis. Microbeam Analysis, 104–160.

Rancourt, D.G. and Ping, J.Y. (1991) Voigt-based methods for arbitrary-shape static hyperfine parameter distribution in Mössbauer spectroscopy. Nuclear Instruments and Methods in Physics Research, B58, 85–97.

Rancourt, D.G., Tume, P., and Lalonde, A.E. (1993) Kinetics of the (Fe^{2+} + OH^-) mica (Fe^{3+} + O^{2-})mica + H oxidation reaction in bulk single-crystal biotite studied by Mössbauer spectroscopy. Physics and Chemistry of Minerals, 20, 276–284.

Rancourt, D.G., Christie, I.A.D., Royer, M., Kodama, H., Robert, J.-L., Lalonde, A.E., and Murad, E. (1994a) Determination of accurate $^4Fe^{3+}$, $^6Fe^{3+}$, and $^6Fe^{2+}$

site populations in synthetic annite by Mössbauer spectroscopy. American Mineralogist, 79, 51–62.
Rancourt, D.G., Ping, J.Y., and Berman, R.G. (1994b) Mössbauer Spectroscopy of Minerals III. Octahedral-site Fe^{2+} quadrupole splitting distributions in the phlogopite-annite series. Physics and Chemistry of Minerals, 21, 258–267.
Rancourt, D.G., Mercier, P.H., Cherniak, D.J., Desgreniers, S., Kodama, H., Robert, J.-L., and Murad, E. (2001) Mechanisms and crystal chemistry of oxidation in annite: resolving the hydrogen-loss and vacancy reactions. Clays and Clay Minerals, 49, 455–491.
Redhammer, G.J. (1998) Characterization of synthetic trioctahedral micas by Mössbauer spectroscopy. Hyperfine Interactions, 117, 85–115.
Redhammer, G.J. and Roth, G. (2002) Single-crystal structure refinements and crystal chemistry of synthetic trioctahedral micas $KM_3(Al^{3+},Si^{4+})_4O_{10}(OH)_2$, where M = Ni^{2+}, Mg^{2+}, Co^{2+}, Fe^{2+}, or Al^{3+}. American Mineralogist, 87, 1464–1476.
Renner, B. and Lehmann, G. (1986) Correlation of angular and bond length distortions in TO_4 units in crystals. Zeitschrift für Kristallographie, 175, 43–59.
Robinson, K., Gibbs, G.V., and Ribbe, P.H. (1971) Quadratic elongation, a quantitative measure of distortion in coordination polyhedra. Science, 172, 567–570.
Russell, R.L. and Guggenheim, S. (1999) Crystal structure of near-end-member phlogopite at high temperature and heat treated Fe-rich phlogopite: the influence of the O, OH, F site. Canadian Mineralogist, 37, 711–720.
Schingaro, E., Mesto, E., Scordari, F., Brigatti, M.F., and Pedrazzi, G. (2005) Cation site partitioning in Ti-rich micas from Black Hill (Australia): a multi-technical approach. Clays and Clay Minerals, 53, 179–189.
Schneider, H. and Eberhard, E. (1990) Thermal expansion of mullite. Journal of the American Ceramic Society, 73, 2073–2076.
Scordari, F., Ventruti, G., Sabato, A., Bellatreccia, F., Della Ventura, G., and Pedrazzi, G. (2006) Ti-rich phlogopite from Mt. Vulture (Potenza, Italy) investigated by a multianalytical approach: substitutional mechanisms and orientation of the OH dipoles. European Journal of Mineralogy, 18, 379–391.
Shannon, R.D. (1976) Revised effective ionic radii and systematic studies of interatomic distances in halides and chalcogenides. Acta Crystallographica, A32, 751–767.
Sheldrick, G.M. (2003): SADABS. University of Göttingen, Germany.
Takeda, H. and Morosin, B. (1975) Comparison of observed and predicted structural parameters of mica at high temperature. Acta Crystallographica, B31, 2444–2452.
Takeda, H. and Ross, M. (1975) Mica polytypism: Dissimilarities in the crystal structures of coexisting 1*M* and $2M_1$ biotite. American Mineralogist, 60, 1030–1040.
Toraya, H. (1981) Distortions of octahedra and octahedral sheets in 1*M* micas and the relation to their stability. Zeitschrift für Kristallographie, 157, 173–190.
Tutti, F., Dubrovinsky, L.S., and Nygren, M. (2000) High temperature study and thermal expansion of phlogopite. Physics and Chemistry of Minerals, 27, 599–603.

Manuscript received May 21, 2007
Manuscript accepted October 10, 2007
Manuscript handled by Warren Huff